

# Effects of Scatter and Attenuation Correction on Quantitative Assessment of Regional Cerebral Blood Flow with SPECT

Hidehiro Iida, Yuichiro Narita, Hirotsugu Kado, Akemi Kashikura, Shigeki Sugawara, Yasuaki Shoji, Toshibumi Kinoshita, Toshihide Ogawa and Stefan Eberl

Departments of Radiology and Nuclear Medicine, Research Institute for Brain and Blood Vessels, Akita, Japan; and Royal Prince Alfred Hospital, Sydney, Australia

Appropriate corrections for scatter and attenuation correction are prerequisites for quantitative SPECT studies. However, in most cerebral SPECT studies, uniform attenuation in the head is assumed, and scatter is usually neglected. This study evaluated the effect of attenuation correction and scatter correction on quantitative values and image contrast. **Methods:** Studies were performed in six normal volunteers (ages 22–26 yr) following intravenous  $^{123}\text{I}$ -IMP administration using a rotating, dual-head gamma camera. A transmission scan was acquired with a  $^{99\text{m}}\text{Tc}$  rod source (74 MBq) placed at the focus of a symmetrical fanbeam collimator. Data were reconstructed using two attenuation coefficient ( $\mu$ ) maps: quantitative  $\mu$  map from the transmission scan and a uniform  $\mu$  map generated by edge detection of the reconstructed images. Narrow and broad beam  $\mu$  values were used with and without scatter correction, respectively. Scatter was corrected with transmission-dependent convolution subtraction and triple-energy window techniques. Quantitative rCBF images were calculated by the previously validated IMP-autoradiographic technique, and they were compared with those obtained by  $^{15}\text{O}$ -water and PET. SPECT and PET images were registered to MRI studies, and rCBF values were compared in 39 ROIs selected on MRI. **Results:** Clear differences were observed in rCBF images between the measured and constant  $\mu$  maps in the lower slices due to the airways and in the higher slices due to increased skull attenuation. However, differences were  $< 5\%$  in all cerebral tissue regions, thus assumption of uniform  $\mu$  introduces little bias. The scatter correction was found to increase the image contrast significantly, i.e., rCBF increased by 20%–30% in gray matter and decreased in white matter regions by 10%–20% after scatter correction, increasing gray-to-white ratio to be close to that of PET measurement. The rCBF values from the two scatter correction were not significantly different, but the triple-energy window technique suffered from increased noise. After scatter correction, rCBF values were in good agreement with those measured by PET. **Conclusion:** This study shows little loss in accuracy results from assuming uniform  $\mu$  map. However, scatter correction is required for the quantitative rCBF values and gray-to-white ratios to approach those of PET.

**Key Words:** iodine-123; regional cerebral blood flow; SPECT; scatter correction; attenuation correction

**J Nucl Med 1998; 39:181–189**

Appropriate corrections for scatter and photon absorption are the main prerequisites for quantitative studies in SPECT. Although there are several studies demonstrating quantitative assessment of cerebral blood flow and other physiological functions in vivo using SPECT, few have applied appropriate scatter and attenuation correction techniques. The scatter distribution adds additional low frequency blurring to the projec-

tion data reducing contrast in the reconstructed images, which is likely to cause systematic underestimation in high count areas and systematic overestimation in low count areas.

Recently, a practical clinical method has been proposed to quantitate quantitative regional cerebral blood flow (rCBF) from a single SPECT scan using  $^{123}\text{I}$ -iodoamphetamine (IMP) (1). We have validated this technique to provide rCBF values that were correlated significantly to those obtained by  $^{15}\text{O}$ -water PET. This method was further validated by a multicenter project involving ten independent institutions showing a good correlation against the existing techniques of  $^{15}\text{O}$ -water PET,  $^{133}\text{Xe}$ -SPECT and  $^{123}\text{I}$ -IMP microsphere analyses (2). However, these studies also demonstrated that rCBF values measured using SPECT were systematically lower in the cortical gray matter regions and systematically greater in the white matter regions. This was also reflected in the low dynamic range for normal average rCBF ranging from 35 ml/min/100g in gray matter to 25 ml/min/100g in white matter. These values resulted in the gray matter-to-white matter ratio of 1/4, which was significantly smaller than those by other techniques such as  $^{15}\text{O}$ -water PET. These observations were partly attributed to lack of scatter correction. In a recent publication, Ichihara et al. (3) demonstrated improved gray/white matter contrast in qualitative  $^{99\text{m}}\text{Tc}$  brain phantom SPECT studies after scatter correction, while Tanaka et al. (4) attributed the reduced contrast to the limited accuracy of conventional attenuation correction methods.

In this study, we evaluated the effects of the scatter correction, as well as appropriate transmission scan based attenuation correction on the rCBF estimation with  $^{123}\text{I}$ -IMP and SPECT. Two independent scatter correction techniques, the triple-energy window (5–7) and transmission dependent convolution subtraction (8–11) were applied to the quantitative  $^{123}\text{I}$ -IMP studies. These techniques are practical to implement clinically and have been extensively investigated (12,13). Reconstructions with measured attenuation coefficients using a transmission source were also compared to data reconstructed with uniform  $\mu$ -maps derived from the reconstructed data using edge detection.

## MATERIALS AND METHODS

### Scatter Correction Methods

Transmission dependent convolution subtraction is a modification of the convolution subtraction method (14) which, rather than assuming a constant scatter fraction ( $k$ ) across the projection, estimates pixel by pixel  $k(x, y)$  values from the transmission data as follows (9–11):

$$k(x, y) = 1 - \frac{1}{A - B \cdot t(x, y)^{\beta/2} + k_0}, \quad \text{Eq. 1}$$

Received Dec. 6, 1996; revision accepted Mar. 25, 1997.

For correspondence or reprints contact: Hidehiro Iida, DSc, Department of Radiology and Nuclear Medicine, Research Institute for Brain and Blood Vessels, 6-10 Senshu-Kubota machi, Akita, Japan.

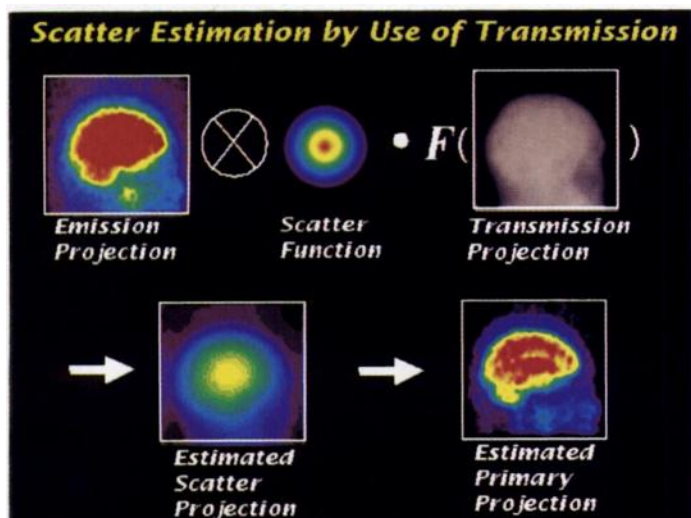


**FIGURE 1.** Transmission-dependent convolution subtraction procedure to compensate scatter in the emission projection data. Geometric means of emission projections were first convolved with an empirically determined scatter function, and were scaled pixel-by-pixel using an empirically defined relation between the scatter fraction and attenuation factor. Two transmission projections were applied in this study: direct measurement of the transmission projection using  $^{99m}\text{Tc}$  source and transmission projection generated from a constant  $\mu$  map in the object. Inverse of the transmission projection is displayed in the figure.

where  $k(x, y)$  is the estimated scatter fraction for pixel  $(x, y)$ ;  $A$ ,  $B$ ,  $\beta$  and  $k_0$  are constants;  $^{123}\text{I}$  equals  $A = 2.4718$ ,  $B = A - 1$ ,  $\beta = 0.20884$ ;  $k_0 = 0.214129$ ;  $t(x, y)$  is the attenuation factor for pixel  $(x, y)$  derived from the transmission projection, i.e.,  $t(x, y) = C(x, y)/C_0$ , where  $C_0$  is the unattenuated transmission count and  $C(x, y)$  is the attenuated transmission count at  $(x, y)$ .

For  $^{123}\text{I}$ , the additional factor  $k_0$  had to be added to the usual  $k(x, y)$  function to account for the septal penetration and scatter in the collimator/detector of the 2% abundance 530 keV emission of  $^{123}\text{I}$  producing apparent scatter outside the head.

The scatter-corrected data  $g(x, y)$  are then given by:

$$g(x, y) = g_{\text{obs}}(x, y) - k(x, y) \cdot (g_{\text{obs}}(x, y) \otimes s), \quad \text{Eq. 2}$$

where  $g_{\text{obs}}(x, y)$  are the observed emission projection data;  $s$  is the scatter function given as the sum of Gaussian and exponential functions (11); and  $\otimes$  denotes convolution integral.

In this study, the attenuation factor  $t(x, y)$  was derived in two ways: (1) From the actual transmission measurement using the rod source and (2) by a forward projecting from assumed constant effective  $\mu$ -values of  $0.166 \text{ cm}^{-1}$  inside the head contour defined by the measured transmission scan. The effective  $\mu$ -value includes contribution from the brain plus the higher density skull. Other parameters and constants were determined experimentally or by Monte Carlo simulations as previously described (11). The transmission dependent convolution subtraction method is graphically illustrated in Figure 1.

The triple energy window technique uses two small (7%) subwindows, just below and above the main photo peak window (20% centered on 159 keV) (5–7). The scatter estimate for the main window is then given by the weighted average of the counts in the subwindows. Spatial smoothing was performed on the subwindow projections as suggested by Ogawa et al. (5,7) and Ichihara et al. (6).

## Subjects

SPECT studies were performed on six normal male volunteers (age range 22–26 yr; mean  $\pm$  1 s.d.;  $24 \pm 1$ ) (Table 1). The healthy status was defined by a medical review of past history of no major disease and physical tests showing no evidence of diabetes mellitus, hypertension or elevated cholesterol levels. The laboratory studies also included screen for serum electrolytes (Na, K, Cl), creatinine and blood urea nitrogen, fasting blood glucose, triglyceride, uric acid and total plasma protein. Three were nonsmokers and the other three were smokers. All volunteers gave written informed consent to the protocol approved by the Ethics Committee of Research Institute for Brain and Blood Vessels-Akita. All subjects underwent brain MRI (T1 and T2 weighted images) and PET scans on the same day as the SPECT scan.

## SPECT Scan

SPECT scans were performed on a dual-head gamma camera fitted with 400 mm focal length, low-energy, high-resolution, symmetric fan-beam collimators. The radius of rotation of 132 mm used in the studies resulted in a reconstructed field of view (FOV) of 22 cm diameter. Only one head was used for the transmission scan, and a 25-cm long  $^{99m}\text{Tc}$  rod source (74 MBq) was placed at the focus of its collimator. Emission scans were performed using both heads. The host computer of this camera was SPARC-20 (Sun Microsystems, Inc., Mountain View, CA), and all data analyses were performed on this workstation.

After a blank scan for 15 min, transmission scans were collected for 15 min. A 60-min dynamic SPECT study was started simultaneously with a 222 MBq, 1 min  $^{123}\text{I}$ -IMP infusion. The SPECT cameras were continuously rotated collecting 60 projections over  $360^\circ$  initially every 15 sec (0.5 sec/projection) and after 10 min, every 30 sec. Three energy windows were selected, i.e., a 20% main window on 159 keV and two additional 7% windows below and above the main window for TEW scatter correction. The projection data for the period of 20 min to 40 min after the  $^{123}\text{I}$ -IMP infusion were summed and used for all further analysis.

## Image Reconstruction

The projection data obtained with the symmetrical fanbeam collimator were first rebinned into parallel projections before any further processing of these data. All image reconstructions were carried out with the ordered-subset ML-EM (OSEM) algorithm (15). The observed spatial resolution was approximately 10 mm FWHM in plane for a line source placed at the center of a cylindrical phantom. OSEM provides similar results as standard EM, but with a typically order of magnitude speed improvement.

**TABLE 1**  
Subjects

| Subject no.     | Age (yr)   | Weight (kg) | Smoke | Heart rate | Systolic blood pressure (mmHg) | PaCO <sub>2</sub> (mmHg) | Hematocrit (%) | Hemoglobin (g/100 ml) |
|-----------------|------------|-------------|-------|------------|--------------------------------|--------------------------|----------------|-----------------------|
| 1               | 25         | 65          | Y     | 76         | 105                            | 40                       | 42             | 14                    |
| 2               | 26         | 73          | N     | 61         | 116                            | 41                       | 50             | 15                    |
| 3               | 24         | 65          | Y     | 55         | 92                             | 39                       | 43             | 14                    |
| 4               | 22         | 60          | N     | 58         | 99                             | 42                       | 44             | 14                    |
| 5               | 24         | 58          | Y     | 57         | 90                             | 47                       | 46             | 15                    |
| 6               | 23         | 56          | N     | 59         | 101                            | 40                       | 46             | 14                    |
| Mean $\pm$ s.d. | $24 \pm 1$ | $63 \pm 6$  |       | $61 \pm 8$ | $101 \pm 9$                    | $41 \pm 3$               | $45 \pm 3$     | $14 \pm 1$            |

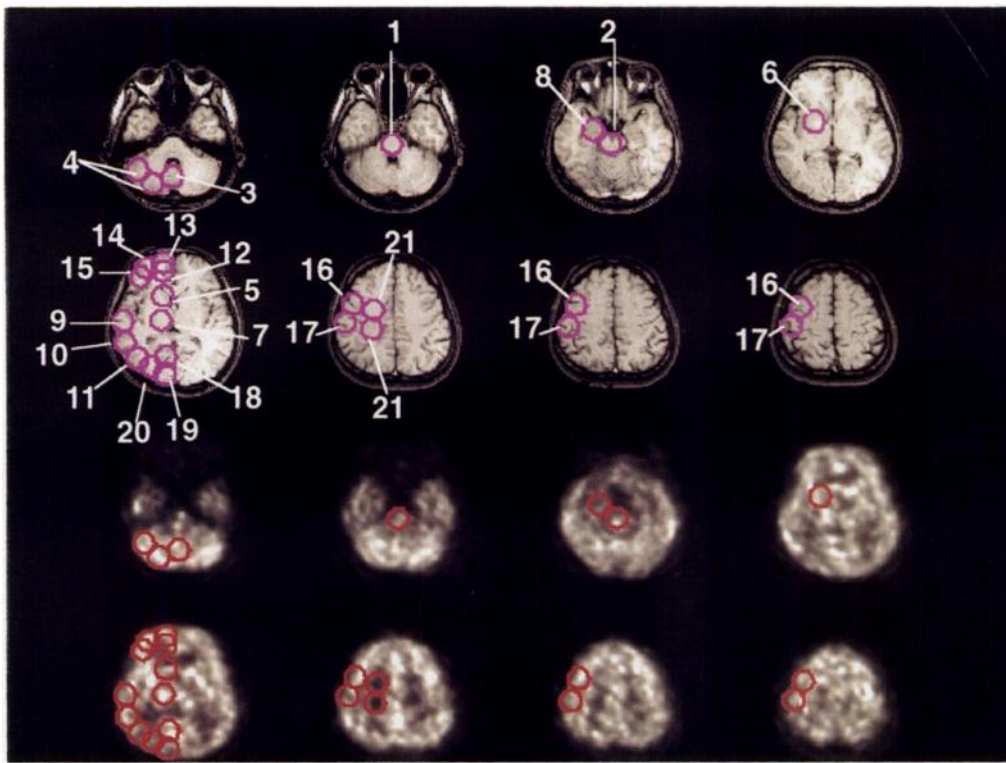


**FIGURE 2.** ROIs selected in this study: (1) pons; (2) mid-brain; (3) cerebellar vermis; (4) cerebellar hemisphere; (5) caudate nucleus; (6) lentiform nucleus; (7) thalamus; (8) hippocampal gyrus; (9–11) superior, middle and inferior temporal gyri, respectively; (12) cingulate gyrus; (13–15) superior, middle and inferior frontal gyri, respectively; (16,17) precentral and postcentral gyri; (18) occipital cuneus, (19,20) posterior and lateral areas of the occipital lobe; (21) semiovale center. Regions on only one hemisphere are shown, but ROIs were also duplicated on the other hemisphere.

Reconstructed transmission  $\mu$ -maps were scaled by a factor of 0.95996 to provide values appropriate for the  $^{123}\text{I}$  photon energy from the  $^{99\text{m}}\text{Tc}$  transmission source. Emission data were reconstructed by two ways using the  $\mu$ -maps derived from the transmission scan and uniform average  $\mu$ -values of  $0.166\text{ cm}^{-1}$  (narrow  $\mu$ ) and  $0.090\text{ cm}^{-1}$  (broad  $\mu$ ) within the head outline defined from the reconstructed images using edge detection. Each  $\mu$ -map was used for both the attenuation correction and the scatter correction when transmission dependent convolution subtraction was applied. To minimize effects of possible movement of the subject between the transmission and emission scans, the head contour was defined using the transmission image.

### Cross Calibration

A cylindrical uniform phantom (16 cm inner diameter, 15 cm in length) was used to calibrate the relative sensitivity of the SPECT scanner against the well counter. Approximately 40 MBq  $^{123}\text{I}$  solution was well-mixed in the phantom, and a SPECT scan was collected for 15 min. A sample was taken from the phantom after the SPECT scan, and its radioactivity concentration was measured using the well counter. This cross calibration scan was performed both at the commencement and after the end of this project. The cross-calibration factor was determined for each reconstruction procedure with each scatter correction technique.

### Calculation of Regional Cerebral Blood Flow by IMP-Autoradiography

SPECT images were corrected for the radioactive decay of  $^{123}\text{I}$  back to the  $^{123}\text{I}$ -IMP injection start time, normalized by the data collection time and cross-calibrated to the well counter. Functional images of rCBF were calculated from a single SPECT scan according to the previously reported IMP-autoradiographic (ARG) method (1,2). The kinetics of  $^{123}\text{I}$ -IMP were modeled by a

single-compartment model, and the influx rate constant ( $K_1$  or rCBF) was calculated according to a table-look-up procedure by assuming a fixed regional distribution volume of  $^{123}\text{I}$ -IMP ( $V_d$ ) of 35 ml/ml (2,16). A single arterial blood sample taken at  $t = 10$  min calibrated the previously-determined standardized input function to obtain the individual arterial input function for each subject (1,2,16).

### PET

All subjects were studied by PET on the same day as the SPECT study and approximately 1 hr before the  $^{123}\text{I}$ -IMP administration. The Headtome V dual PET scanner (Shimadzu Corp., Kyoto, Japan) was used (17), which provides 47 tomographic slices for the brain and 31 slices for the heart. The intrinsic spatial resolution was 4.0 mm FWHM in-plane and 4.3 mm FWHM axially. With the Butterworth filter used in the image reconstruction, the observed image resolution was approximately 8 mm FWHM in-plane. Two tomographic slices were added before the reconstruction, yielding an axial resolution of approximately 7.5 mm FWHM.

After a transmission scan for attenuation correction, a 180-sec scan was performed following a continuous infusion of  $^{15}\text{O}$ -labeled water ( $\text{H}_2^{15}\text{O}$ ) over 2 min. The functional rCBF images were calculated according to the  $\text{H}_2^{15}\text{O}$  autoradiography (18,19). The distribution volume of water was assumed to be 0.80 ml/ml (20). The arterial input function was obtained from the left ventricular time-activity curve in the heart scanner according to a previous validated procedure (21,22).

### Data Analysis

CBF images obtained from the PET and the  $^{123}\text{I}$ -IMP-SPECT studies were registered to the MRI image of each subject using an automated image registration program (23).

A total of 39 regions of interest (ROIs) were drawn on both

**TABLE 2**  
Summary Results of Regional CBF Values (ml/min/100g)

|                      | IMP SPECT rCBF (ARG)         |                              |                             |                              |                 |
|----------------------|------------------------------|------------------------------|-----------------------------|------------------------------|-----------------|
|                      | TDCS + TCT $\mu$             | TDCS + narrow $\mu$          | NoSC + broad $\mu$          | TEW + TCT $\mu$              | PET rCBF        |
| Brain stem           |                              |                              |                             |                              |                 |
| pons                 | 30.5 $\pm$ 5.2 <sup>¶</sup>  | 34.4 $\pm$ 5.6               | 31.1 $\pm$ 4.0              | 30.0 $\pm$ 3.9               | 33.8 $\pm$ 9.3  |
| midbrain             | 29.5 $\pm$ 7.2 <sup>¶</sup>  | 32.3 $\pm$ 7.4               | 31.5 $\pm$ 6.1              | 29.9 $\pm$ 8.0               | 34.8 $\pm$ 11.1 |
| Cerebellum           |                              |                              |                             |                              |                 |
| vermis               | 40.2 $\pm$ 11.7              | 40.4 $\pm$ 10.1              | 32.3 $\pm$ 5.6*             | 37.1 $\pm$ 9.4               | 44.1 $\pm$ 10.9 |
| right hemisphere     | 45.1 $\pm$ 10.4*             | 42.1 $\pm$ 7.4               | 32.5 $\pm$ 5.0*             | 41.4 $\pm$ 9.0               | 45.9 $\pm$ 15.7 |
| left hemisphere      | 45.7 $\pm$ 10.0 <sup>†</sup> | 43.2 $\pm$ 6.7               | 32.7 $\pm$ 4.1*             | 39.7 $\pm$ 6.8               | 49.6 $\pm$ 16.4 |
| Caudate              |                              |                              |                             |                              |                 |
| right                | 35.4 $\pm$ 7.7*              | 38.7 $\pm$ 7.9               | 35.9 $\pm$ 5.3*             | 36.0 $\pm$ 7.2               | 40.6 $\pm$ 14.0 |
| left                 | 41.0 $\pm$ 10.7 <sup>†</sup> | 45.0 $\pm$ 12.4              | 39.3 $\pm$ 7.1              | 41.8 $\pm$ 8.4*              | 39.7 $\pm$ 5.7  |
| Lentiform            |                              |                              |                             |                              |                 |
| right                | 38.4 $\pm$ 7.2 <sup>†</sup>  | 42.2 $\pm$ 6.8               | 38.3 $\pm$ 5.6*             | 39.7 $\pm$ 7.4*              | 45.8 $\pm$ 10.8 |
| left                 | 41.1 $\pm$ 8.9*              | 45.0 $\pm$ 10.3              | 39.5 $\pm$ 6.7*             | 42.9 $\pm$ 8.0               | 45.8 $\pm$ 11.1 |
| Thalamus             |                              |                              |                             |                              |                 |
| right                | 38.6 $\pm$ 9.4*              | 43.1 $\pm$ 9.8               | 39.0 $\pm$ 6.7              | 40.9 $\pm$ 8.6               | 44.3 $\pm$ 8.9  |
| left                 | 35.6 $\pm$ 10.3              | 38.7 $\pm$ 11.1              | 36.7 $\pm$ 7.1              | 37.4 $\pm$ 10.3              | 38.0 $\pm$ 9.3  |
| Temporal             |                              |                              |                             |                              |                 |
| right hippocampus    | 26.4 $\pm$ 5.8 <sup>†</sup>  | 28.7 $\pm$ 6.0               | 28.1 $\pm$ 4.4              | 25.9 $\pm$ 5.5               | 32.8 $\pm$ 9.8  |
| sup temp gy          | 44.4 $\pm$ 13.1 <sup>†</sup> | 42.7 $\pm$ 11.1 <sup>†</sup> | 35.2 $\pm$ 6.8 <sup>†</sup> | 42.7 $\pm$ 12.0 <sup>†</sup> | 52.0 $\pm$ 12.9 |
| mid temp gy          | 39.0 $\pm$ 10.8 <sup>§</sup> | 36.9 $\pm$ 8.4 <sup>‡</sup>  | 30.6 $\pm$ 5.9 <sup>†</sup> | 36.2 $\pm$ 10.3 <sup>†</sup> | 42.6 $\pm$ 9.2  |
| inf temp gy          | 33.5 $\pm$ 7.7*              | 30.9 $\pm$ 7.1               | 26.1 $\pm$ 4.2 <sup>†</sup> | 30.3 $\pm$ 6.3               | 33.7 $\pm$ 6.6  |
| left hippocampus     | 24.7 $\pm$ 5.3 <sup>†</sup>  | 26.5 $\pm$ 5.3               | 27.3 $\pm$ 4.0              | 25.3 $\pm$ 4.7               | 28.4 $\pm$ 9.5  |
| sup temp gy          | 41.2 $\pm$ 9.3*              | 40.4 $\pm$ 9.4*              | 33.3 $\pm$ 6.0 <sup>‡</sup> | 39.5 $\pm$ 7.6*              | 44.3 $\pm$ 6.7  |
| mid temp gy          | 37.6 $\pm$ 8.8               | 36.1 $\pm$ 8.1               | 30.6 $\pm$ 4.6*             | 35.1 $\pm$ 6.3               | 40.2 $\pm$ 9.1  |
| inf temp gy          | 34.5 $\pm$ 7.8               | 32.2 $\pm$ 6.9               | 27.4 $\pm$ 4.2*             | 31.1 $\pm$ 5.7               | 35.5 $\pm$ 9.5  |
| Frontal              |                              |                              |                             |                              |                 |
| right cingulate      | 31.0 $\pm$ 9.1               | 32.6 $\pm$ 9.0               | 29.7 $\pm$ 5.7              | 29.2 $\pm$ 7.1               | 33.5 $\pm$ 10.4 |
| sup fro gy           | 39.0 $\pm$ 10.0              | 39.0 $\pm$ 8.7               | 33.1 $\pm$ 5.3*             | 37.4 $\pm$ 7.6               | 38.7 $\pm$ 9.7  |
| mid fro gy           | 38.0 $\pm$ 9.2               | 38.1 $\pm$ 8.1               | 31.1 $\pm$ 5.4*             | 34.3 $\pm$ 8.0               | 37.9 $\pm$ 10.5 |
| inf fro gy           | 39.6 $\pm$ 8.5               | 40.6 $\pm$ 7.3               | 32.7 $\pm$ 4.8              | 36.6 $\pm$ 7.4               | 37.6 $\pm$ 12.1 |
| precentral           | 41.6 $\pm$ 7.7               | 40.0 $\pm$ 6.9               | 32.6 $\pm$ 4.2*             | 39.3 $\pm$ 6.0               | 42.8 $\pm$ 10.2 |
| left cingulate       | 28.8 $\pm$ 9.0 <sup>†</sup>  | 31.0 $\pm$ 9.5               | 28.2 $\pm$ 6.0              | 26.6 $\pm$ 6.7               | 30.4 $\pm$ 7.5  |
| sup fro gy           | 37.1 $\pm$ 8.0               | 38.6 $\pm$ 7.1               | 32.4 $\pm$ 5.1*             | 34.9 $\pm$ 6.9               | 39.1 $\pm$ 9.2  |
| mid fro gy           | 36.6 $\pm$ 9.8               | 36.5 $\pm$ 8.7               | 29.7 $\pm$ 5.3*             | 33.9 $\pm$ 7.5               | 36.3 $\pm$ 9.5  |
| inf fro gy           | 38.0 $\pm$ 9.3               | 38.9 $\pm$ 8.9               | 31.7 $\pm$ 5.5              | 35.4 $\pm$ 7.4               | 41.2 $\pm$ 15.2 |
| precentral           | 40.9 $\pm$ 9.5*              | 38.8 $\pm$ 8.7               | 31.8 $\pm$ 5.7*             | 38.7 $\pm$ 7.6               | 39.2 $\pm$ 9.5  |
| Parietal             |                              |                              |                             |                              |                 |
| right postcentral    | 37.7 $\pm$ 6.9               | 35.6 $\pm$ 6.2               | 30.4 $\pm$ 4.5*             | 36.6 $\pm$ 6.1               | 37.3 $\pm$ 7.1  |
| left postcentral     | 37.6 $\pm$ 8.8               | 35.4 $\pm$ 7.6               | 30.4 $\pm$ 5.2*             | 36.6 $\pm$ 7.3               | 37.1 $\pm$ 8.5  |
| Occipital            |                              |                              |                             |                              |                 |
| right cuneus         | 42.1 $\pm$ 10.2 <sup>†</sup> | 42.5 $\pm$ 10.2 <sup>†</sup> | 35.3 $\pm$ 6.2 <sup>†</sup> | 40.9 $\pm$ 8.7 <sup>†</sup>  | 50.6 $\pm$ 11.3 |
| post occ area        | 34.3 $\pm$ 9.0*              | 31.4 $\pm$ 8.5*              | 26.2 $\pm$ 5.5 <sup>†</sup> | 31.6 $\pm$ 6.9*              | 38.1 $\pm$ 7.8  |
| lateral occ area     | 31.1 $\pm$ 8.1*              | 28.6 $\pm$ 7.3*              | 24.7 $\pm$ 4.1 <sup>‡</sup> | 28.6 $\pm$ 5.4*              | 32.8 $\pm$ 5.3  |
| left cuneus          | 40.9 $\pm$ 9.6*              | 41.8 $\pm$ 9.6*              | 35.2 $\pm$ 6.5*             | 40.2 $\pm$ 9.9*              | 47.8 $\pm$ 11.6 |
| post occ area        | 33.8 $\pm$ 8.5*              | 30.9 $\pm$ 8.0*              | 26.1 $\pm$ 5.2 <sup>†</sup> | 30.6 $\pm$ 6.2*              | 35.3 $\pm$ 7.0  |
| lateral occ area     | 31.4 $\pm$ 7.6 <sup>¶¶</sup> | 29.0 $\pm$ 7.1               | 24.8 $\pm$ 4.9*             | 27.6 $\pm$ 6.8               | 29.6 $\pm$ 7.8  |
| Smioval center       |                              |                              |                             |                              |                 |
| right                | 22.7 $\pm$ 6.1               | 23.8 $\pm$ 6.1               | 25.1 $\pm$ 4.4*             | 21.7 $\pm$ 6.0               | 22.4 $\pm$ 3.6  |
| left                 | 23.9 $\pm$ 5.4               | 25.1 $\pm$ 5.8               | 25.9 $\pm$ 3.8*             | 23.1 $\pm$ 4.4               | 22.5 $\pm$ 5.4  |
| Total average        | 36.1 $\pm$ 8.0               | 36.4 $\pm$ 7.5               | 31.4 $\pm$ 4.9*             | 34.5 $\pm$ 6.5               | 38.2 $\pm$ 8.8  |
| Cortical gray matter | 36.2 $\pm$ 8.2               | 35.5 $\pm$ 7.5               | 30.2 $\pm$ 4.9 <sup>†</sup> | 34.0 $\pm$ 6.6               | 37.5 $\pm$ 8.4  |
| Deep gray matter     | 38.4 $\pm$ 8.6*              | 42.1 $\pm$ 9.2               | 38.1 $\pm$ 6.1*             | 39.8 $\pm$ 7.7               | 43.2 $\pm$ 10.0 |
| White matter         | 23.3 $\pm$ 5.7               | 24.5 $\pm$ 5.8               | 25.5 $\pm$ 4.0 <sup>‡</sup> | 22.4 $\pm$ 5.0               | 22.5 $\pm$ 4.4  |
| Cerebellum           | 43.7 $\pm$ 10.5*             | 41.9 $\pm$ 7.9               | 32.5 $\pm$ 4.8*             | 39.4 $\pm$ 8.2               | 47.2 $\pm$ 14.2 |

\*p < 0.05.

<sup>†</sup>p < 0.01.

<sup>‡</sup>p < 0.001 vs. PET.

<sup>§</sup>p < 0.001 for TDCS with TCT vs. TEW.

<sup>¶</sup>p < 0.001 for TDCS with TCT vs. TDCS with constant  $\mu$ .

Average and s.d. are listed for each ROI (n = 6).



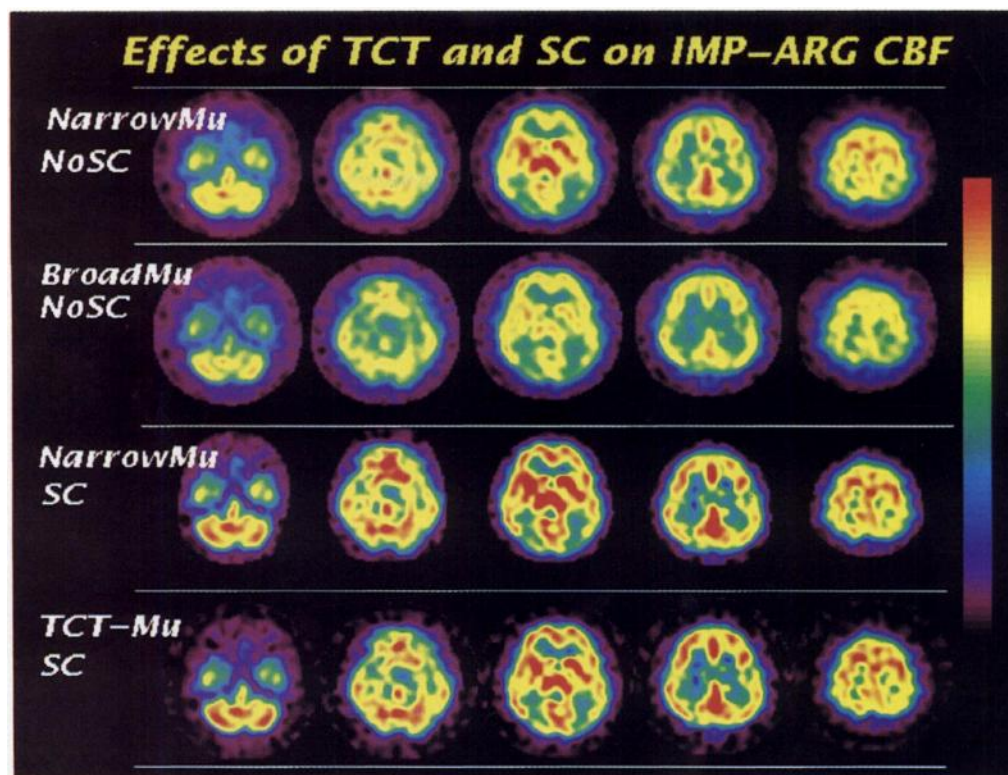


**FIGURE 3.** Comparison of rCBF images calculated from  $^{123}\text{I}$ -IMP SPECT. The top row shows images without scatter correction using a narrow beam  $\mu$  value. The second from top row shows images without scatter correction using a broad beam  $\mu$  value. The third from top row shows images with scatter correction by the TDCS method using a constant narrow beam  $\mu$  value of  $0.166\text{ cm}^{-1}$ . The bottom row shows images with scatter correction by TDCS using the measured  $\mu$  map.

hemispheres on the MRI images and then superimposed onto the registered SPECT study (Fig. 2, Table 2). The criteria of ROI selection followed Yamagichi's work (24). All ROIs had a diameter of 20 mm.

All data were presented as mean  $\pm$  1 s.d. Paired data were compared according to the paired Student t-test with Bonferoni correction and  $p < 0.05$  was considered statistically significant.

## RESULTS

Quantitative average  $\mu$  value for  $^{99\text{m}}\text{Tc}$  obtained from the cross-calibration phantom was  $0.147 \pm 0.006\text{ cm}^{-1}$  in the area of water (which is consistent with the scatter-free attenuation  $\mu$ -value in water). For human studies, the  $\mu$  value (average and s.d. of six studies) was  $0.155 \pm 0.007\text{ cm}^{-1}$  in the cerebral tissue and  $0.197 \pm 0.0010\text{ cm}^{-1}$  in the bone (parietal skull). The mean  $\mu$  value inside the head outline (apparent  $\mu$  value) was  $0.166 \pm 0.010\text{ cm}^{-1}$  at a level of the anterior commissure-posterior commissure (AC-PC) line.

The effect of scatter correction and assumed  $\mu$ -value on rCBF estimation with  $^{123}\text{I}$ -IMP is demonstrated in Figure 3. No scatter correction and narrow beam  $\mu$  value resulted in relatively higher rCBF values in the deep structures. Broad beam  $\mu$  values provided relatively homogeneous rCBF distribution throughout the cortical and deep gray matter regions with clearly reduced image contrast. Scatter correction substantially improved image contrast. The increase of rCBF values was typically 30% in the cerebellum and approximately 20% in the temporal, frontal, parietal and occipital regions, but only small in the deep gray matter regions. There was no apparent difference between the rCBF images obtained by using the directly measured  $\mu$  map and those using a constant narrow beam  $\mu$  map. However, ratio images between measured and assumed constant  $\mu$ -value corrected reconstructions showed differences up to 30% (Fig. 4). The differences were greatest in

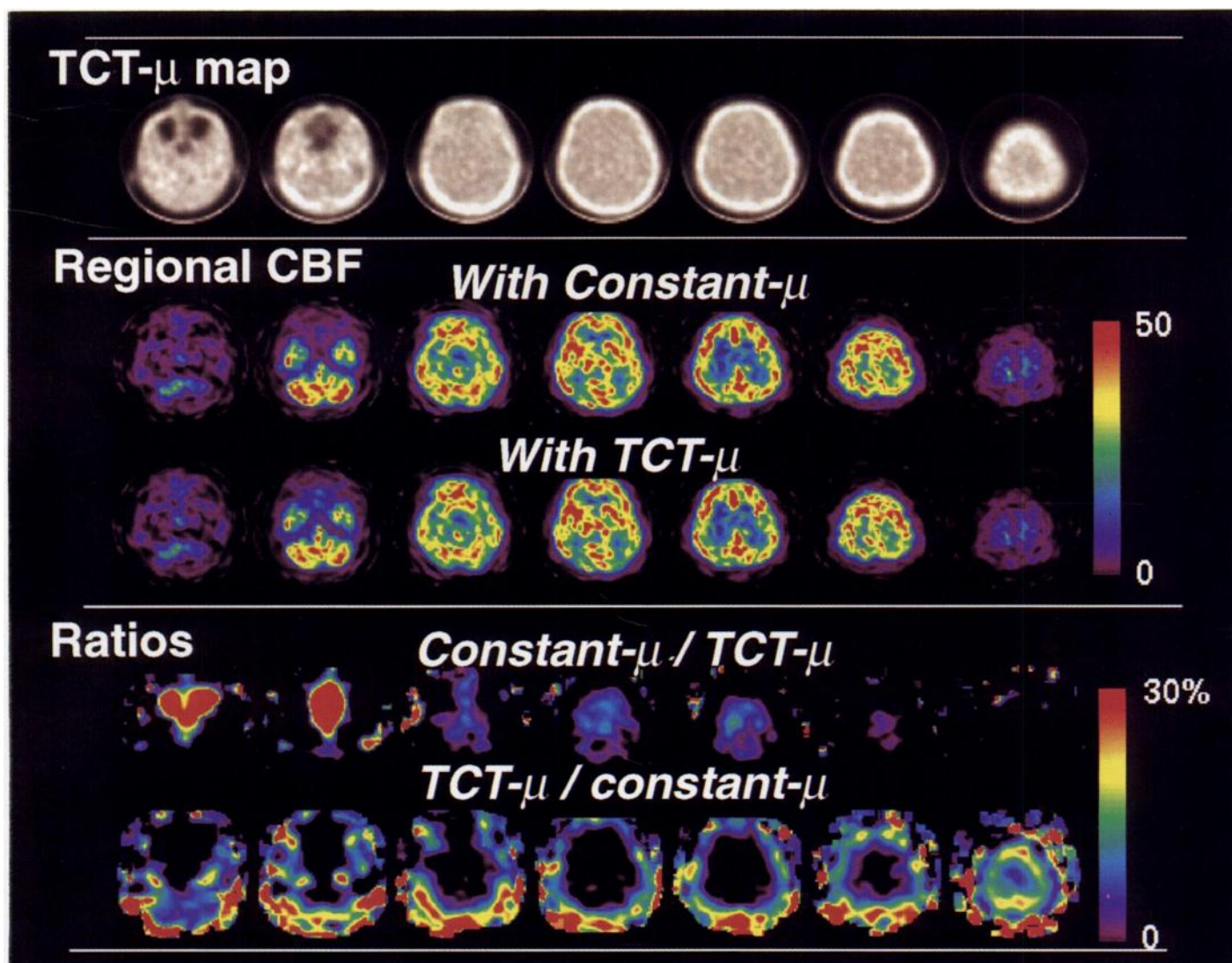
the lower slices due to the airways and in higher slices with increased skull thickness. However, the biggest differences were mainly confined to extra-cerebral areas.

Figure 5 shows the apparent  $\mu$  values (an average over whole-brain slice) at each tomographic slice level parallel to the AC-PC plane. The apparent  $\mu$  value decreased toward the lower slices, which was due to inclusion of the airway in the ROI, but increased at higher levels, which was attributed to the relatively thicker skull. This slice dependent change of the apparent  $\mu$  value was, however, smaller than the inter-subject variation observed in this study.

Figure 6 shows a typical comparison of rCBF images obtained by the  $^{123}\text{I}$ -IMP SPECT with those from the  $\text{H}_2^{15}\text{O}$  PET in one of the studies. Although the image contrast was slightly higher in PET images, good agreement between PET and SPECT rCBF images was apparent.

Table 2 summarizes rCBF values obtained for each ROI described in Figure 2 as well as results of the statistical analysis. Quantitative rCBF values obtained by the  $^{123}\text{I}$ -IMP SPECT using the measured  $\mu$  map showed significant differences from those using a constant  $\mu$  map in ten ROIs. Systematic overestimation was found in areas of the pons, midbrain and hippocampus regions by a factor of 7%–10% when using a constant  $\mu$  map compared with the use of measured  $\mu$  map. Significant underestimation was observed in some occipital areas by a factor of 5%–8%. However, rCBF values were not significantly different in other regions, and there was good agreement between the use of measured and constant  $\mu$  maps for a wide rCBF range as demonstrated in Figure 7.

Quantitative rCBF values obtained by the  $^{123}\text{I}$ -IMP SPECT were highly dependent on the scatter correction (Fig. 8). Significant underestimation was found in several cortical areas without scatter correction such as the temporal, frontal, parietal



**FIGURE 4.** Quantitative  $\mu$ -images (top row) and rCBF images obtain from a typical study. Regional CBF images were calculated using the  $\mu$  maps measured with the transmission scan (second row) and also using a constant  $\mu$  images generated by detecting the edge of the head (third row). The ratios of these two rCBF images were also calculated (bottom two rows).

and occipital regions as well as in the cerebellum (Table 2). In contrast, white matter regions tended to be overestimated without scatter correction. Scatter correction with either trans-

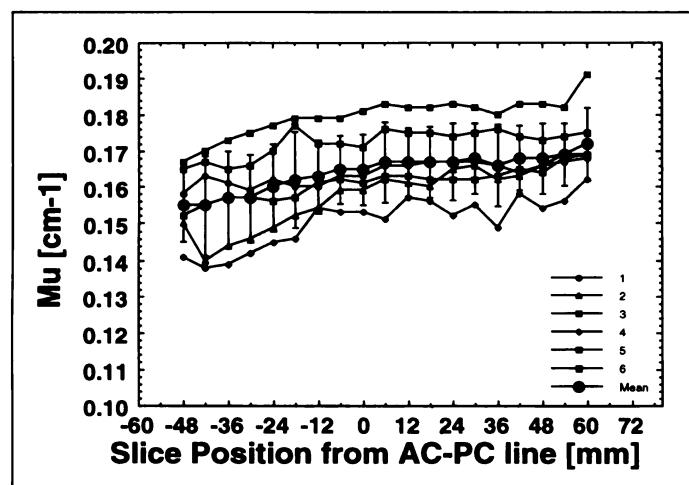


**FIGURE 5.** Apparent  $\mu$  values (an average inside the head outline) for various tomographic slice levels parallel to the AC-PC-plane obtained from all six studies.

mission dependent convolution subtraction or triple energy window eliminated most of the systematic bias reducing the number of regions with SPECT rCBF that were significantly different from PET rCBF. Although rCBF is still systematically underestimated at a high flow range (by a factor of 8%–10%), the scatter correction improved the agreement with the PET rCBF values, and increased the correlation coefficient in Figure 8.

The underestimation of average slice CBF without scatter correction depended on the slice level. It ranged from –25% for low slices at the level of the cerebellum and Semioval centre to 0% at the midlevel and –30% for the highest slices. This is attributed to the cross-sectional size of the object, i.e., the size of the scattering material.

Shown in Figure 9 is a comparison of rCBF images obtained in a volunteer study with the  $^{123}\text{I}$ -IMP using transmission dependent convolution subtraction with those using triple energy window. Although images were clearly noisier with triple energy window, rCBF images were visually in good agreement between the two methods. Part of the temporal and occipital areas, as well as in the cerebellum, showed significant differences between the two scatter correction methods by a factor of approximately 7% at maximum



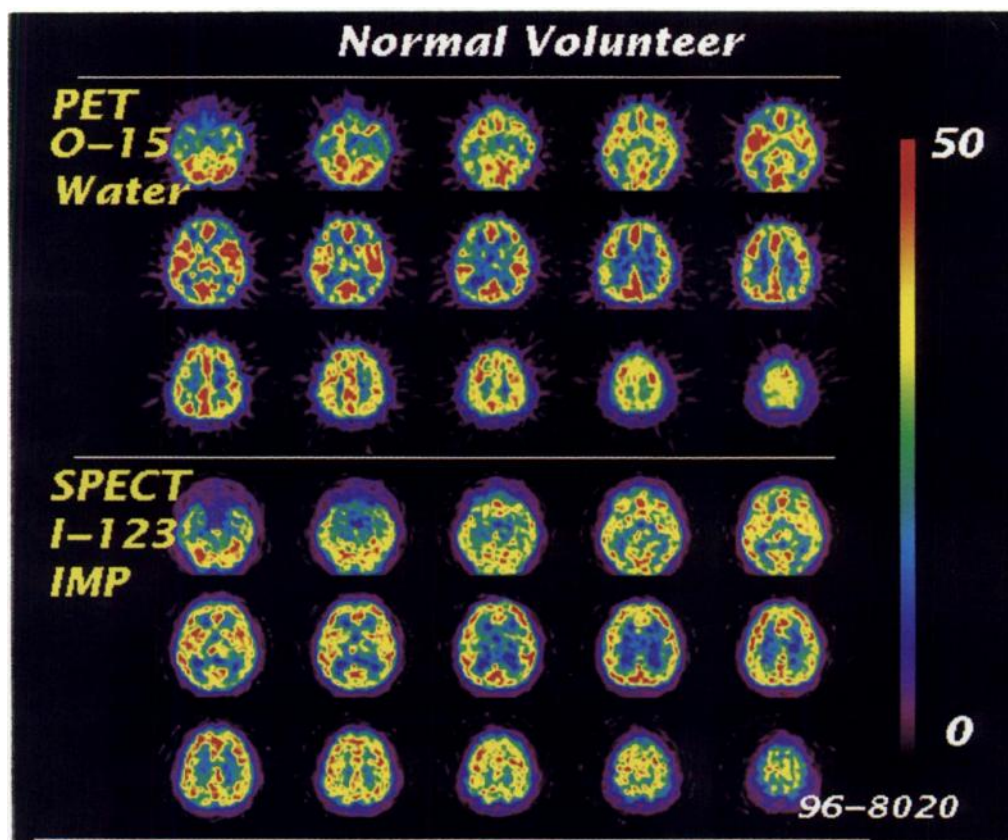


**FIGURE 6.** Comparison of rCBF images obtained by  $\text{H}_2^{15}\text{O}$  PET with those by  $^{123}\text{I}$ -IMP SPECT in a typical study. Note that the same absolute color scale calibrated in ml/min/100g was used for both images.

(Table 2), but good agreement can be seen globally as shown in Figure 10.

## DISCUSSION

In this study, we found that (a) scatter correction improved contrast between gray and white matter flow and largely eliminated the underestimation of flow in gray matter and

overestimation in white matter; (b) scatter correction improved agreement between  $^{123}\text{I}$ -IMP SPECT flow and  $\text{H}_2^{15}\text{O}$  PET flow measurements; (c) loss of accuracy was small when using constant  $\mu$ -value maps compared to measured attenuation coefficients; and (d) there was little difference in accuracy between triple energy window and transmission dependent convolution subtraction scatter correction techniques. However, triple energy window correction resulted in noisier images.

The cortical gray-to-white matter  $^{123}\text{I}$ -IMP CBF ratio increased from 1.18 without scatter correction to 1.55 with scatter correction approaching the ratio of 1.67 obtained with  $\text{H}_2^{15}\text{O}$  PET. The increase in ratio with scatter correction was due to both a reduction in white matter flow and an increase in gray matter flow, which after scatter correction, were not significantly different from the PET  $\text{H}_2^{15}\text{O}$  flow values. However, the gray/white matter ratio for both the scatter-corrected SPECT and the PET measurements are lower than expected. This is mainly attributed to the relatively large ROIs (20-mm diameter) used, causing inclusion of both gray and white matter in individual regions. The poorer spatial resolution of SPECT should cause some underestimation of gray matter flow due to increased partial volume effect. However, this effect is also reduced in our ROI analysis by the large ROIs used, but may be responsible at least partly for the differences seen on the rCBF images.

The first-pass extraction fraction of  $^{123}\text{I}$ -IMP has not been directly measured as has been done for  $\text{H}_2^{15}\text{O}$  (25). Our good agreement between scatter corrected  $^{123}\text{I}$ -IMP SPECT and  $\text{H}_2^{15}\text{O}$  PET rCBF values (discrepancy was <10% at the highest rCBF) suggests that the first-pass extraction fraction of  $^{123}\text{I}$ -IMP may be greater than expected and close to that for  $\text{H}_2^{15}\text{O}$ . It is worth noting that the first-pass extraction

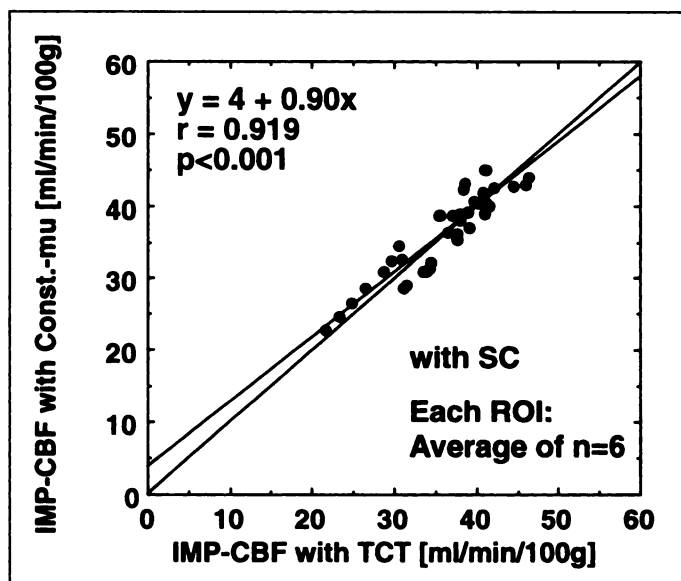


**FIGURE 7.** Comparison of quantitative rCBF values obtained with TDCS using a constant  $\mu$  map with those using a measured  $\mu$  map. Each value correspond to an average of six studies in each ROI described in Figure 2. See also Table 2.

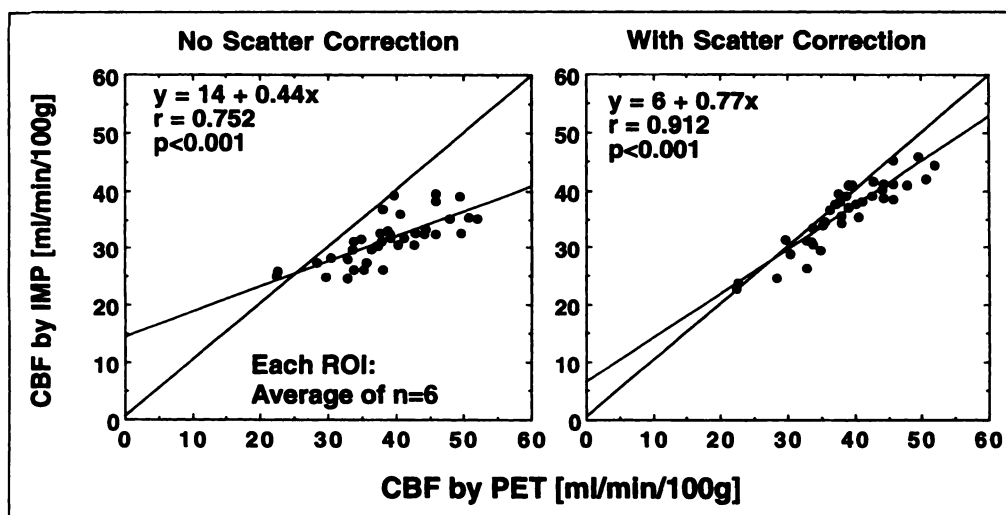


**FIGURE 8.** Comparison of rCBF values obtained by  $^{123}\text{I}$ -IMP SPECT and those by  $\text{H}_2^{15}\text{O}$  PET without (left) and with (right) scatter correction by TDCS. Each value corresponds to an average of six studies in each ROI described in Figure 2. See also Table 2.

fraction is also limited in  $\text{H}_2^{15}\text{O}$ , and therefore, the two tracers might have similar value of the extraction fraction.

Unlike in cardiac studies, it is less common to perform measured attenuation correction in brain SPECT studies. Instead, a constant  $\mu$ -value inside the head outline is frequently assumed for attenuation correction. We demonstrated in this study that constant  $\mu$  attenuation maps can be used with little loss of accuracy in rCBF estimates in most brain regions. In this study, we determined the head outline from the transmission scan. The transmission scan is usually not available when using constant  $\mu$ -value and, instead, the head outline has to be determined from the emission scan. In a preliminary analysis using edge detection on the emission data, we found systematic errors at high cortical levels of 3–5 mm if the same threshold level was assumed for the whole data, which can cause errors in rCBF of the order of 5%–10%. Further studies are, therefore, required in optimally defining the edge of the head surface using only the emission data and assuming a thickness for the skull as proposed for PET-FDG studies (26). Alternatively, the head outline could also be determined from the co-registered MRI study, if available.

We have shown, in our recent studies, that triple energy window has limited accuracy when the activity is localized in a heterogeneous absorption object (27). This study demonstrated that triple energy window provides accurate scatter correction

for  $^{123}\text{I}$ -IMP SPECT of the brain in which activity is distributed relatively diffusely in a fairly homogeneous absorption object. The validity of triple energy window in the brain study has also been shown previously by Ljungberg et al. (12) by Monte Carlo simulation. Transmission dependent convolution subtraction provided similar scatter correction accuracy as triple energy window, but it introduced substantially less noise into the rCBF images compared with triple energy window. One potential disadvantage of the transmission dependent convolution subtraction is its requirement for transmission data. We have shown in this study that accurate scatter correction with transmission dependent convolution subtraction can also be achieved by generating transmission projection data from the assumed constant  $\mu$ -maps.

The effects of the scatter were dependent on the area in the brain. Scatter correction had the largest effect in areas of the cerebellum, temporal and occipital cortex, when compared with PET rCBF. This is thought to be due to these areas having a relatively small amount of scatter compared with other regions. Use of the broad beam  $\mu$  value, which assumes a certain amount of scatter (consistent with the cross-calibration phantom experiment), undercorrects for attenuation in these regions and results in reduced counts (and rCBF) in these areas. This error may also be of particular importance when analysing kinetic data that is dynamically changing over time because the scatter component

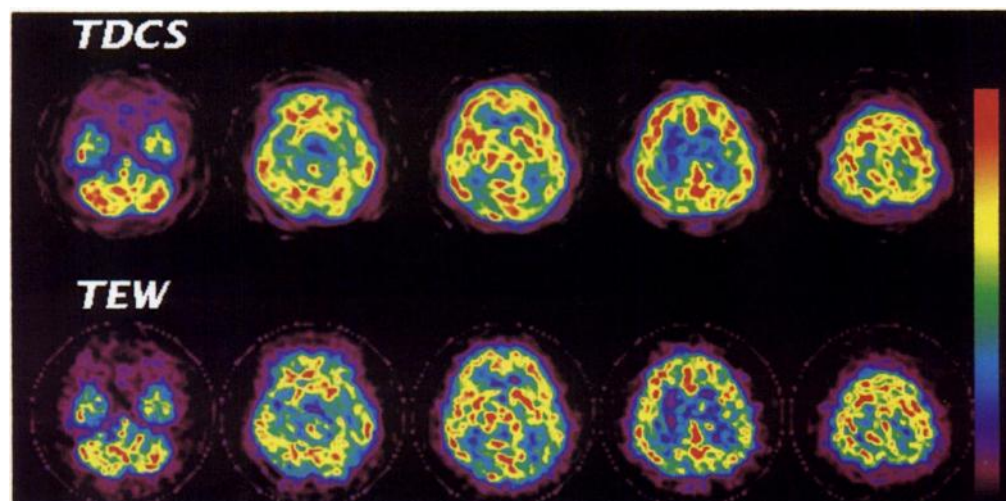


**FIGURE 9.** Comparison of TDCS versus TEW rCBF images calculated from  $^{123}\text{I}$ -IMP SPECT study. The increased image noise in the TEW corrected images is clearly apparent.



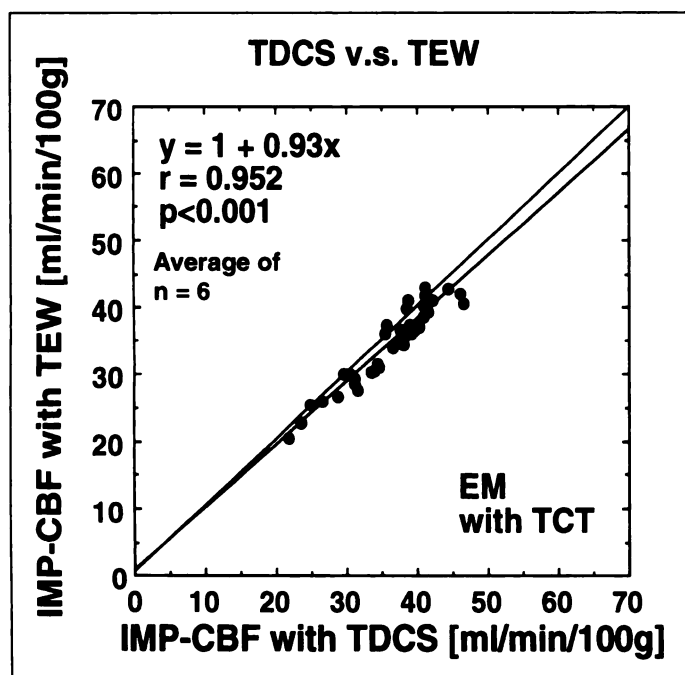


**FIGURE 10.** Plot of rCBF values obtained by  $^{123}\text{I}$ -IMP SPECT using TDCS versus those using TEW. Each value corresponds to an average of six studies in each ROI described in Figure 2. See also Table 2.

is dependent not only on the object geometry, but it is also dependent the distribution of radioactivity in other regions.

Transmission dependent convolution subtraction takes into account the spatial distribution of the scatter material in the FOV using information obtained from the transmission data to estimate pixel-by-pixel scatter fraction in addition to taking into account the emission source distribution. This is the major difference from the conventional convolution-subtraction method (9,10). This not only applies to the measured transmission data, but also to the transmission data derived from forward-projecting assumed constant  $\mu$ -values. This study demonstrated that, despite a relatively large variation of observed  $\mu$ -value between slices (as well as among subjects), a good agreement can be obtained by assuming a constant  $\mu$ -value within the head contour. This is probably attributed to the fact that the scatter fraction reaches a plateau at large attenuation factors (9,10). Reasons for the intersubject variation of the  $\mu$ -value are unknown (most likely due to the error in the measurement system). Slice dependency of the averaged  $\mu$ -value is probably due to the effective thickness of the bone.

## CONCLUSION

This study has found, with appropriate scatter and attenuation corrections, excellent agreement between  $^{123}\text{I}$ -IMP SPECT and the gold standard  $\text{H}_2^{15}\text{O}$  PET rCBF values can be achieved. This study did not demonstrate the need for transmission scans for brain studies. Systematic errors introduced by assuming a constant  $\mu$  in the object were observed only in particular regions and were relatively small. The  $^{123}\text{I}$ -IMP SPECT method described in this article is a practical method for calculating accurate, quantitative rCBF images in a routine clinical setting.

## ACKNOWLEDGMENTS

We wish to thank Dr. Yuko Miura, from Department of Radiology and Nuclear Medicine, Research Institute for Brain and

Blood Vessels, Akita, for invaluable advice on the data analysis. We are also indebted to the staff of Research Institute for Brain and Blood Vessels, Akita. We thank Richard Larkin from the Department of Statistics, Macquarie University, Australia, and Brian Hutton from Westmead Hospital, Australia, for the use of the OSEM software and for their input regarding its implementation.

## REFERENCES

1. Iida H, Itoh H, Nakazawa M, et al. Quantitative mapping of regional cerebral blood flow using iodine-123-IMP and SPECT. *J Nucl Med* 1994;35(suppl. b):2019-2030.
2. Iida H, Akutsu T, End K, et al. A multi-center validation of regional cerebral blood flow quantitation using I-123 iodoamphetamine and single photon emission computed tomography. *J Cereb Blood Flow Metab* 1996;16:781-793.
3. Ichihara T, Motomura N, Ogawa K, Hasegawa H, Hashimoto J, Kubo A. Evaluation of SPET quantification of simultaneous emission and transmission imaging of the brain using a multidetector SPET system with the TEW scatter compensation method and fan-beam collimation. *Euro J Nucl Med* 1996;23:1292-1299.
4. Tanaka E, Toyama H, Murayama H. Convolution image reconstruction from quantitative single photon emission computed tomography. *Phys Med Biol* 1984;29:1489-1500.
5. Ogawa K, Harata Y, Ichihara T, Kubo A, Hashimoto S. A practical method for position-dependent Compton-scatter correction in single photon emission CT. *IEEE Trans Med Imag* 1991;10:408-412.
6. Ichihara T, Ogawa K, Motomura N, Kubo A, Hashimoto S. Compton scatter compensation using the triple-energy window method for single- and dual-isotope SPECT. *J Nucl Med* 1993;34:2216-2221.
7. Ogawa K, Ichihara T, Kubo A. Accurate scatter correction in single photon emission CT. *Ann Nucl Med Sci* 1994;7:145-150.
8. Bailey DL, Hutton BF, Meikle SR, Fulton RR, Jackson CB. Iterative scatter correction incorporating attenuation data [Abstract]. *Eur J Nucl Med* 1989;15:542.
9. Meikle SE, Hutton BF, Bailey DL, Fulton RR, Schindhelm K. SPECT scatter correction in non-homogeneous media. *Information processing in medical imaging: 12th international conference*. Berlin: Springer-Verlag; 1991:34-44.
10. Meikle SR, Hutton BF, Bailey DL. A transmission dependent method for scatter correction in SPECT. *J Nucl Med* 1994;35:360-367.
11. Narita Y, Eberl S, Iida H, et al. Monte Carlo and experimental evaluation of accuracy and noise properties of two scatter correction methods for SPECT. *Phys Med Biol* 1996;41:2481-2496.
12. Ljungberg M, King MA, Hademenos GJ, Strand S-E. Comparison of four scatter correction methods using Monte Carlo simulated source distributions. *J Nucl Med* 1994;35:143-151.
13. Buvat I, Rodriguez-Villafuerte M, Todd-Popropek A, Benali H, Di Paola R. Comparative assessment of nine scatter correction methods based on spectral analysis using Monte Carlo simulations. *J Nucl Med* 1995;36:1476-1488.
14. Axelsson B, Msaki P, Israelsson A. Subtraction of compton-scattered photons in single-photon emission computerized tomography. *J Nucl Med* 1984;25:490-494.
15. Hudson HM, Larkin RS. Accelerated image reconstruction using ordered subsets of projection data. *IEEE Trans Med Imag* 1994;MI-13:601-609.
16. Iida H, Itoh H, Bloomfield PM, et al. A method to quantitate cerebral blood flow using a rotating gamma camera and iodine-123 iodoamphetamine with one blood sampling. *Euro J Nucl Med* 1994;21:1072-1084.
17. Iida H, Miura S, Kanno I, Ogawa T, Uemura K. A new PET camera for noninvasive quantitation of physiological functional parametric images: Headtome-V-dual. In: Myers R, Cunningham V, Bailey D, Jones T, eds. *Quantification of brain function: PET*. San Diego, CA: Academic Press, Inc., 1996:57-61.
18. Raichle ME, Martin WRW, Herscovitch P, Markham J. Brain blood flow measured with intravenous  $\text{H}_2^{15}\text{O}$ . II. Implementation and validation. *J Nucl Med* 1983;24:790-798.
19. Kanno I, Iida H, Miura S, et al. A system for cerebral blood flow measurement using an  $\text{H}_2^{15}\text{O}$  autoradiographic method and positron emission tomography. *J Cereb Blood Flow Metab* 1987;7:143-153.
20. Iida H, Kanno I, Miura S. Rapid measurement of cerebral blood flow with positron emission tomography. *Exploring brain function anatomy with positron tomography*. Wiley Chichester, London: CIBA Foundation Symposium 163, 1991:23-42.
21. Iida H, Rhodes CG, de Silva R, et al. Use of the left ventricular time-activity curve as a noninvasive input function in dynamic oxygen-15-water positron emission tomography. *J Nucl Med* 1992;33:1669-1677.
22. Iida H, Higano S, Tomura N, et al. Evaluation of regional difference of tracer appearance time in cerebral tissues using  $^{15}\text{O}$ water and dynamic positron emission tomography. *J Cereb Blood Flow Metab* 1988;8:285-288.
23. Ardekani BA, Braun M, Hutton BF, Kanno I, Iida H. A fully automatic multimodality image registration algorithm. *J Comp Assist Tomogr* 1995;19:615-623.
24. Yamaguchi T, Kanno I, Uemura K, et al. Reduction in regional cerebral metabolic rate of oxygen during human aging. *Stroke* 1986;17:1220-1228.
25. Eichling JO, Raichle ME, Grubb RL. In: Ter-Pogossian MM, ed. Evidence of the limitations of water as a freely diffusible tracer in brain in the rhesus monkey. *Circ Res* 1974;35:358-364.
26. Bergstrom M, Litton J, Eriksson L, Bohm C, Blomqvist G. Determination of object contour from projections for attenuation correction in cranial positron emission tomography. *J Comput Assist Tomogr* 1982;6:365-372.
27. Narita Y, Iida H, Eberl S, Nakamura T. Monte Carlo evaluation of accuracy and noise properties of two scatter correction methods. *IEEE Trans Med Image* 1997;in press.